The Astrophysical Journal, 824:47 (13pp), 2016 June 10 doi:10.3847/0004-637X/824/1/47

COHERENT EVENTS AND SPECTRAL SHAPE AT ION KINETIC SCALES IN THE FAST SOLAR WIND TURBULENCE

Sonny Lion, Olga Alexandrova, and Arnaud Zaslavsky
LESIA, Observatoire de Paris, PSL Research University, CNRS, Sorbonne Universités, UPMC Univ. Paris 06, Univ. Paris Diderot, Sorbonne Paris Cité, France; sonny.lion@obspm.fr
Received 2015 July 11; accepted 2016 March 16; published 2016 June 9

ABSTRACT

In this paper we investigate spectral and phase coherence properties of magnetic fluctuations in the vicinity of the spectral transition from large, magnetohydrodynamic to sub-ion scales using in situ measurements of the *Wind* spacecraft in a fast stream. For the time interval investigated by Leamon et al. (1998) the phase coherence analysis shows the presence of sporadic quasi-parallel Alfvén ion cyclotron (AIC) waves as well as coherent structures in the form of large-amplitude, quasi-perpendicular Alfvén vortex-like structures and current sheets. These waves and structures importantly contribute to the observed power spectrum of magnetic fluctuations around ion scales; AIC waves contribute to the spectrum in a narrow frequency range whereas the coherent structures contribute to the spectrum over a wide frequency band from the inertial range to the sub-ion frequency range. We conclude that a particular combination of waves and coherent structures determines the spectral shape of the magnetic field spectrum around ion scales. This phenomenon provides a possible explanation for a high variability of the magnetic power spectra around ion scales observed in the solar wind.

Key words: magnetic fields – methods: data analysis – plasmas – solar wind – turbulence – waves

1. INTRODUCTION

In typical hydrodynamic (HD) flow, a turbulence cascade develops between energy injection and energy dissipation scales and its spectrum $\sim k^{-5/3}$ can be described by Kolmogorov's phenomenology (Kolmogorov 1941). The coherent structures, responsible for intermittency, are filaments of vorticity that are localized in space but cover all scales, from the energy injection scale up to the dissipation scale $\ell_{\rm d}$, i.e., their cross section is of the order of $\ell_{\rm d}$ (Frisch 1995). The situation is mostly the same for magnetohydrodynamic turbulence, where the absence of characteristic scales gives rise to a well defined power-law behavior of the spectrum of turbulent fluctuations. Dissipative processes are in this case related to the plasma resistivity, and coherent structures, responsible for intermittency, are usually current sheets with a thickness of the order of $\ell_{\rm d}$.

However, in the solar wind, the resistivity and the viscosity are extremely low, and turbulence can develop down to characteristic scales of the plasma before being dissipated. The first range of characteristic scales encountered are the ion kinetic scales, such as ion cyclotron frequency $f_{ci} = q_i B_0/2\pi m_i$ (B_0 being the mean magnetic field), the ion Larmor radius $\rho_i = v_{{\rm th}\perp i}/2\pi f_{ci}$, with ion thermal speed $v_{{\rm th}\perp i} = \sqrt{2k_B T_{\perp i}/m_i}$ ($T_{\perp i}$ being the ion temperature perpendicular to $\boldsymbol{B}_0$), and the ion inertial length $\lambda_i = c/\omega_{{\rm p}i}$ (the ion plasma frequency is defined as $\omega_{{\rm p}i} = q_i\sqrt{n_i/\epsilon_0 m_i}$, ϵ_0 being the permittivity of free space). Observations show that the Kolmogorov-like cascade ends at these scales, and the spectrum is observed to be steeper at smaller scales, exhibiting another power-law behavior in the so-called kinetic range (e.g., Alexandrova et al. 2013). In between these two power-law regimes lies the so-called transition range, around the ion characteristic scales. The spectral shape of this transition region is quite variable. It can sometimes be adequately fitted by a power law (as was done, e.g., in Smith et al. 2006 or in Sahraoui et al. 2010), but it sometimes exhibits a non-power-law smooth transition behavior, as observed by Bruno & Trenchi (2014), for example, or even positive slopes in the presence of quasi-monochromatic waves (Jian et al. 2014).

Several authors studied this transition range by introducing a break frequency $f_{\rm b}$, defined as the upper boundary of the Kolmogorov cascade. This frequency was usually determined to be the intersection of slopes obtained by independent linear fits of the lower and upper frequency parts of the spectrum (e.g., Bourouaine et al. 2012). Furthermore, numerous studies attempted to correlate the break frequency $f_{\rm b}$ with ion plasma characteristic scales in order to determine which physical process controls the spectral steepening. This includes, for example, the studies of Leamon et al. (2000), Markovskii et al. (2008), Perri et al. (2010), Bourouaine et al. (2012), and Bruno & Trenchi (2014). But these authors do not agree on which scale, if any, is best correlated with $f_{\rm b}$, and therefore which process governs the physics of the spectral steepening.

Our purpose here is to study which physical processes are at work around ion scales, how these processes influence the spectral shape at these scales, and therefore why the transition region does sometimes exhibit a clear spectral break and sometimes not. To do this, we chose to re-analyze a fast solar wind interval used in Figure 1 of Leamon et al. (1998) wherein a sharp and well defined break was observed. We use the Morlet wavelet transform, which gives us the possibility to have information on the local phase of the signal. Using this tool, we show that the clear spectral break at the frequency $f_{\rm b} \simeq 0.4$ Hz results from the superimposition of (i) non-coherent and unpolarized fluctuations, (ii) emissions of parallel propagating Alfvén ion cyclotron (AIC) waves in a narrow frequency range around $f_{\rm b}$, and (iii) large-amplitude coherent structures in the form of Alfvén vortex-like structures and current sheets. These structures cover a very large range of scales in the inertial range; their smallest scale, or their characteristic size, appears to be a few λ_i or ρ_i, which is close to $f_{\rm b}$ by the Doppler shift.

Our work also sheds light on the nature of intermittency in the solar wind. Previous studies showed the role of planar

structure like current sheets, rotational discontinuities and shocks in solar wind intermittency (Veltri 1999; Salem et al. 2009; Greco et al. 2012; Perri et al. 2012). Here, we point out that besides current sheets and rotational discontinuities, we find also the signature of vortex-like structures at ion scales, indicating that our vision of solar wind intermittency was too restricted to planar structures and ignored filamentary structures like vortices.

Our results clearly show, as well, that the physics of solar wind turbulence around ion scales is not governed by a single physical process. Because the proportion of structures, waves, and non-coherent fluctuations is not always the same and depends on local phenomena (wave instabilities) and non-local ones (convection of structures), the spectral shape may vary from time to time. These results may help to explain why the break is not a permanent feature in the solar wind and also why there is no single characteristic scale that controls the spectral steepening at ion scales (as it is usually defined).

The paper is organized as follows. Section 2 describes the spacecraft data and summarizes the plasma parameters as well as the spectral properties of the selected interval; Section 3 includes the identification and characterization of the most energetic and polarized magnetic fluctuations of the time interval. In Section 4, we detail the spectral contribution of waves, coherent structures, and the rest of the signal by using the wavelet coherency technique. Finally, Section 5 summarizes our findings and brings our conclusions.

2. OVERVIEW OF INTERVAL

We consider here an interval of two hours [12:30:00–14:30:00] UTC on 1995 January 30 of measurements of the local magnetic field vector obtained by the MFI instrument (Lepping et al. 1995) on board the *Wind* spacecraft with a resolution of 184 ms; we use also the 92 s resolution proton data from the SWE instrument (Ogilvie et al. 1995). Since these magnetic field and proton measurements are not evenly spaced in time and have time gaps, we interpolated all the data to the resolution of 184 ms for MFI and 92 s for SWE. All vector data are given in the geocentric solar ecliptic (GSE) reference frame.

Figure 1 shows the plasma parameters in the studied time interval, in the following order: the three components of the magnetic field $\boldsymbol{B}$, the three components of the velocity vector $\boldsymbol{V}$, the angle θ_{BV} between $\boldsymbol{B}$ and $\boldsymbol{V}$, the proton density N, the total proton temperature T (blue line), perpendicular $T_\perp$ (red line) and parallel $T_\parallel$ (purple line) proton temperatures ($\parallel/\perp$ with respect to the mean magnetic field $\boldsymbol{B}_0$), the plasma parameters $\beta = nkT/(B^2/2\mu_0)$ (purple line) and $\beta_\parallel = nkT_\parallel/(B^2/2\mu_0)$ (red line), and the temperature anisotropy $T_\perp/T_\parallel$ (blue line). The central interval between 13:00:00 and 14:00:00 UTC delimited by dashed lines is the interval used in Figure 1 of Leamon et al. (1998). Two areas of interest discussed below are indicated by gray filled bands.

Table 1 summarizes the parameters of the plasma in the central interval. In particular, it can be noted that the mean velocity corresponds well to the fast wind stream $|\boldsymbol{V}_0| = (691 \pm 12)\,\mathrm{km\,s^{-1}}$. Moreover the field-to-flow angle is $\theta_{BV} = (143 \pm 17)^\circ$, which implies that $\boldsymbol{B}_0$ nearly follows the Parker spiral (Parker 1958) and is directed sunward. The complete interval presents similar characteristics.

The spectrum of the central interval (between 13:00:00 and 14:00:00 UTC) is presented in the upper panel of Figure 2 as a function of the frequency in the spacecraft frame. The black curve shows the total power spectral density (PSD) calculated with the continuous wavelet transform (see Equation (4) in Appendix A), the filled area represents its 95% confidence

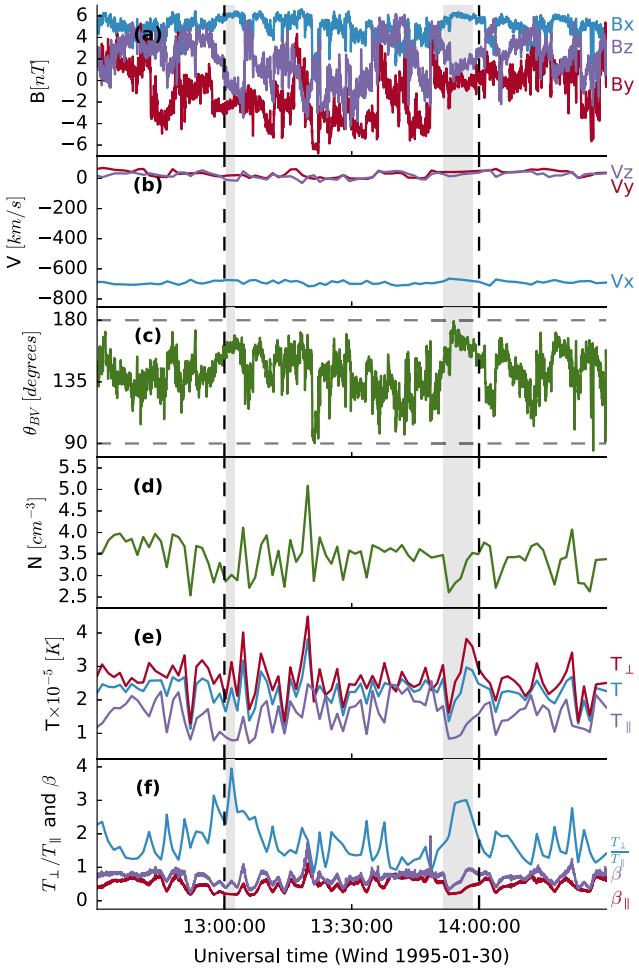

Figure 1. Time series of solar wind data as measured by the *Wind* spacecraft on 1995 January 30. From the top down, the six panels show (a) the vector magnetic field $\boldsymbol{B}$, (b) the vector proton velocity $\boldsymbol{V}$, (c) the angle between $\boldsymbol{B}$ and $\boldsymbol{V}$, (d) the proton density, (e) the proton total, parallel, and perpendicular temperatures, with respect to the mean magnetic field, and (f) the plasma ion β, $\beta_\parallel$, and temperature anisotropy ($T_\perp/T_\parallel$). Gray filled bands represent two areas where AIC waves are present (as shown in Section 3). The central interval between the two dashed lines corresponds to Figure 1 of Leamon et al. (1998) and is used here for the spectral analysis, whereas the entire interval is used for the rest of the study.

Table 1
Average Plasma Parameters between 13:00:00 and 14:00:00 UTC, on 1995 January 30, as Measured by the *Wind* Spacecraft

B (nT)	6.3 ± 0.2 (0.8, −0.2, 0.3)
V (km s^{-1})	691 ± 12 (−0.998, 0.045, 0.032)
θ_{BV} (deg)	143 ± 17
N(cm^{-3})	3.4 ± 0.4
T (K)	(22.8 ± 3.9) × 10^4
$T_\perp/T_\parallel$	1.8 ± 0.6
β; $\beta_\parallel$	0.7 ± 0.2; 0.5 ± 0.2
ρ_i (km)	108 ± 10
λ_i (km)	124 ± 6
f_{ci} (Hz)	0.096 ± 0.003

Note. Unit vectors are given in brackets in the GSE reference frame.

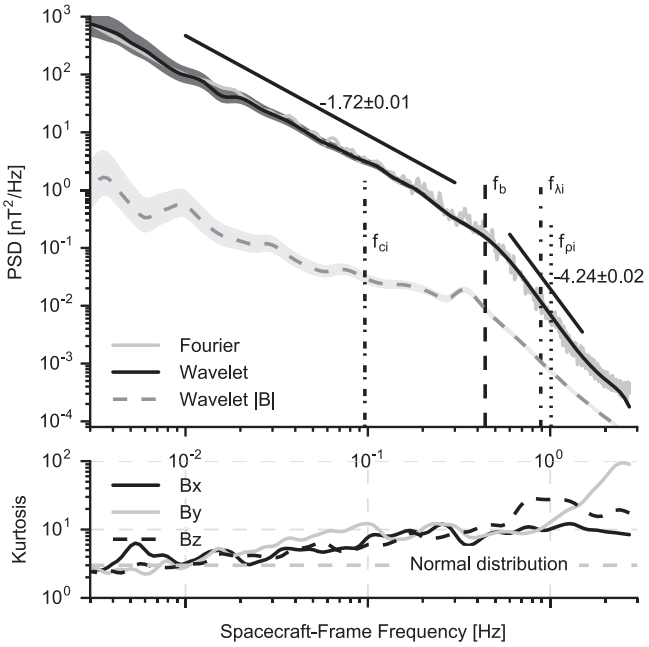

Figure 2. Upper panel: total power spectral density of the magnetic field (solid lines) as a function of frequency in the spacecraft frame as measured by *Wind* on 1995 January 30, from 13:00 to 14:00 UTC, computed with FFT (gray) and Morlet wavelet (black) algorithms. The spectrum of compressible magnetic fluctuations (gray dashed line) is computed from the magnetic field modulus with Morlet wavelets, PSD($|\boldsymbol{B}|$). Straight lines show power-law fits. Vertical lines indicate the break frequency f_b (dashed), the ion cyclotron frequency f_{ci} (dashed–dotted, left), as well as the inertial length $f_{\lambda i}$ (dashed–dotted, right) and the Larmor radius $f_{\rho i}$ (dotted) Doppler-shifted to spacecraft frequency using the Taylor hypothesis (Taylor 1938). Lower panel: kurtosis for each component of the magnetic field computed from wavelet coefficients. The horizontal dashed line indicates the value of 3 expected for a normal distribution. The bump in PSD($|\boldsymbol{B}|$) at 0.33 Hz and the oscillations of the kurtosis of B_x and B_y are due to the spinning frequency of the *Wind* spacecraft.

interval (Equation (7)), while the gray curve shows, for comparison, the total spectrum calculated with a windowed Fourier transform by applying a pre-whitening and post-darkening, as was done by, e.g., Leamon et al. (1998) and Bieber et al. (1993). The dashed line shows the spectrum of the magnetic field modulus $B = |\boldsymbol{B}|$, which is used as a proxy for the compressible fluctuations. Again, the filled area represents the 95% confidence interval. One can notice that the confidence interval is negligible compared to the thickness of the curve for frequencies higher than 0.1 Hz. For the other spectra of this paper, the confidence intervals are almost the same as in Figure 2.

Spectra end at ∼2.7 Hz, the Nyquist frequency of the MFI data of this interval. At frequencies $f > 1.6$ Hz there appears a flattening of the spectrum caused by the contribution from instrumental noise. The probe's spin at 0.33 Hz is not visible on the total spectrum, but appears in the modulus spectrum as an excess of energy around that frequency. The break frequency $f_b \simeq 0.44$ Hz as well as characteristic plasma frequencies $f_{ci} \simeq 0.096$ Hz, $f_{\lambda i} = \frac{V}{2\pi\lambda_i} \simeq 0.89$ Hz, and $f_{\rho i} = \frac{V}{2\pi\rho_i} \simeq 1.0$ Hz are indicated by vertical lines. Note that the ion characteristic scales cover, in this case, one decade in frequency, ∼[0.1, 1] Hz.

We also show power-law fitting for frequency ranges $[10^{-2}, 0.3]$ Hz (inertial range) and [0.6, 1.6] Hz (transition range), respectively, $f^{-1.72}$ and $f^{-4.25}$. These results are similar to those obtained by Leamon et al. (1998). We note that $f^{-4.25}$ is obtained for a very short frequency interval. The break frequency f_b is near the plasma characteristic frequencies but does not match any of them.

The lower panel of Figure 2 shows the kurtosis (Zwillinger & Kokoska 2000; Jones et al. 2001) for three components of the magnetic field in the GSE frame as a function of the frequency. Within the inertial range, the kurtosis of the three components increases with the frequency, as expected for an intermittent turbulent cascade. At ion scales, the kurtosis of the three components changes its behavior: it shows a plateau. Such a plateau around ion scales has already been observed in the solar wind by Alexandrova et al. (2008) and Wu et al. (2013). Then at sub-ion scales, the kurtosis of the B_y component increases again, while for B_x and B_z the plateau continues. However, at these high frequencies the measurements are too close to the instrumental noise to give any firm conclusions. The ratio between the spectrum of compressible fluctuations and the total PSD, the so-called compressibility index (not shown here), increases with increasing frequency as one approaches the ionic scales, as already observed by Alexandrova et al. (2008), Salem et al. (2012), and Kiyani et al. (2013).

3. IDENTIFICATION OF WAVES AND STRUCTURES

The spectra give a global vision of the properties of an interval but do not allow one to distinguish between the different processes at work, which can appear at different times. In contrast, wavelet spectrograms (or scalograms) allow one to follow the energy evolution of the magnetic field fluctuations in the time–frequency (or time–scale) space (Farge 1992; Farge & Schneider 2015).

We use hereafter scalograms compensated by the inertial range spectrum observed here $\propto f^{-1.7}$ (see Figure 2). This compensation allows one to see more clearly variations of the magnetic energy relative to the background.

We use also the flow-field reference frame defined as follows:

$$\begin{aligned} \boldsymbol{e}_z &= \boldsymbol{B}_0/|\boldsymbol{B}_0| \\ \boldsymbol{e}_x &= \boldsymbol{e}_z \times \boldsymbol{V}_0/|\boldsymbol{V}_0| \\ \boldsymbol{e}_y &= \boldsymbol{e}_z \times \boldsymbol{e}_x. \end{aligned} \quad (1)$$

Compensated scalograms of perpendicular and parallel energy of magnetic fluctuations, $(|W_x(f, t)|^2 + |W_y(f, t)|^2) \times f^{1.7}$ and $|W_z(f, t)|^2 \times f^{1.7}$, are presented, respectively, in Figures 3(a) and (b) as functions of time and timescale $\tau = 1/f$. Figure 3(c) shows a cut of the parallel and perpendicular scalograms at 0.1 Hz (10 s). Finally Figure 3(d) shows the polarization map in the plane perpendicular to $\boldsymbol{B}_0$ built with the phase differences $\Delta\Phi_{xy}(f, t)$ between B_x and B_y (see Equation (8) in Appendix A), in the way of a scalogram where blue and red areas represent the left-handed and right-handed polarized fluctuations, respectively, and black/white is used for the linear polarization.

The scalograms show clearly high-energy events that span almost all frequencies, for example around 13:37:00 UTC. This coupling over many scales is an intrinsic property of coherent structures (Frisch 1995; Alexandrova et al. 2013). The scalogram of the parallel component also reveals an excess of energy around 0.33 Hz (3 s), a signature of the probe spin. This excess is only visible in the parallel fluctuations because, as shown in the scalograms, the perpendicular components are

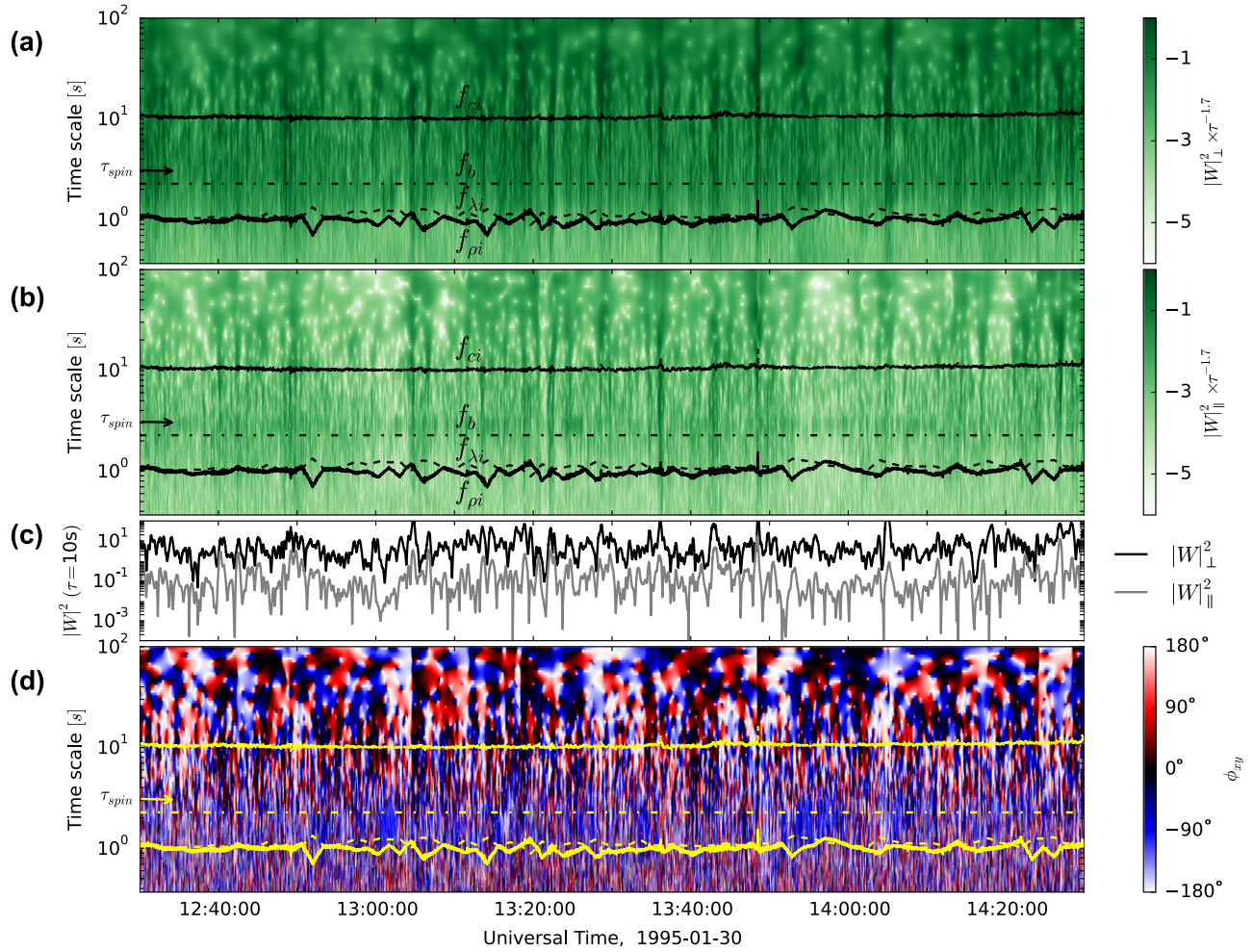

Figure 3. Time evolution of magnetic field fluctuations. (a) Compensated scalogram of the energy of transverse fluctuations, $(|W_x(f, t)|^2 + |W_y(f, t)|^2) \times f^{1.7}$, as a function of time and timescale $\tau = 1/f$; black solid and dashed–dotted lines indicate f_b, f_{ci}, $f_{\lambda i}$, and $f_{\rho i}$; an arrow indicates the spin timescale $\tau_{spin} = 3$ s of the *Wind* spacecraft. (b) The same as (a) but for the parallel fluctuations $|W_z(f, t)|^2 \times f^{1.7}$. (c) A cut of perpendicular (black) and parallel (gray) scalograms at $f = 0.1$ Hz ($\tau = 10$ s). (d) Phase differences between B_x and B_y calculated using complex Morlet wavelets, $\Delta\Phi_{xy}(t, \tau)$, which give a polarization map in the plane perpendicular to $\boldsymbol{B}_0$, as a function of time and timescales.

more energetic than the parallel one. The energy of the magnetic fluctuations is lower at the edges of the central interval (around 13:00 and 14:00 UTC) mainly for the parallel component. These properties are especially visible in Figure 3(c) and we see that $10 \leqslant \frac{|W_\perp|^2}{|W_\parallel|^2} \leqslant 100$ during the whole interval.

Finally the polarization map (Figure 3, bottom panel) shows that the phase differences fluctuate greatly and seem, at first sight, distributed almost randomly. However, we observe at the beginning (13:00:30 to 13:02:30 UTC) and at the end (13:51:30 to 13:58:30 UTC) of the central interval two events indicated by gray bands on Figure 1, during which the polarization remains around $-90°$ at frequencies around f_b (horizontal yellow dashed–dotted line). These events correspond to left-handed polarized waves in the magnetic field reference frame and appear when the turbulence background level and especially $W_\parallel^2$ are the lowest (see Figure 3(c)). The first wave lasts 2 minutes (13:00:30 to 13:02:30 UTC) with a frequency between 0.4 and 1 Hz (or timescales $\tau \in [1, 2.5]$ s). The local spectrum, calculated over these 2 minutes, has a bump in this frequency range (not shown). Here, $\boldsymbol{B}$ and $\boldsymbol{V}$ are almost parallel ($\theta_{BV} \simeq 160°$). Using the minimum variance analysis (Sonnerup & Scheible 1998) and assuming that the wavevector $\boldsymbol{k}$ is in the minimum variance direction $\boldsymbol{e}_{\min}$, we obtain that the angle $\theta_{kB} \simeq 14°$, i.e., that $\boldsymbol{k}$ and $\boldsymbol{B}_0$ are almost parallel. The second wave, which lasts 7 minutes (13:51:30 to 13:58:30 UTC), has similar properties.

Figure 4 provides magnetic field fluctuations of the three components filtered between $f_{\min} = 0.4$ Hz and $f_{\max} = 1$ Hz for a 30 s time interval within the first left-handed Alfvén wave emission. Fluctuations are defined as

$$\delta B_j = L_{f_{\max}}(B_j) - L_{f_{\min}}(B_j),\ j = x, y, z, \qquad (2)$$

where L_{fs} is the moving average at frequency f_s (window of size $1/f_s$). The left panel shows the time evolution of the fluctuations, while the right panel shows the hodogram of fluctuations in the plane perpendicular to $\boldsymbol{B}_0$ in the time interval Δt_1 (indicated in the left panel). Fluctuations of the perpendicular components are of the same intensity and with a phase shift of $-\pi/2$, which results in a left-handed (with respect to $\boldsymbol{B}_0$), almost circular rotation in the hodogram. Maximum and intermediate eigenvalues of the minimum variance matrix are almost equal ($\lambda_{\text{med}}/\lambda_{\max} \sim 0.8$), while

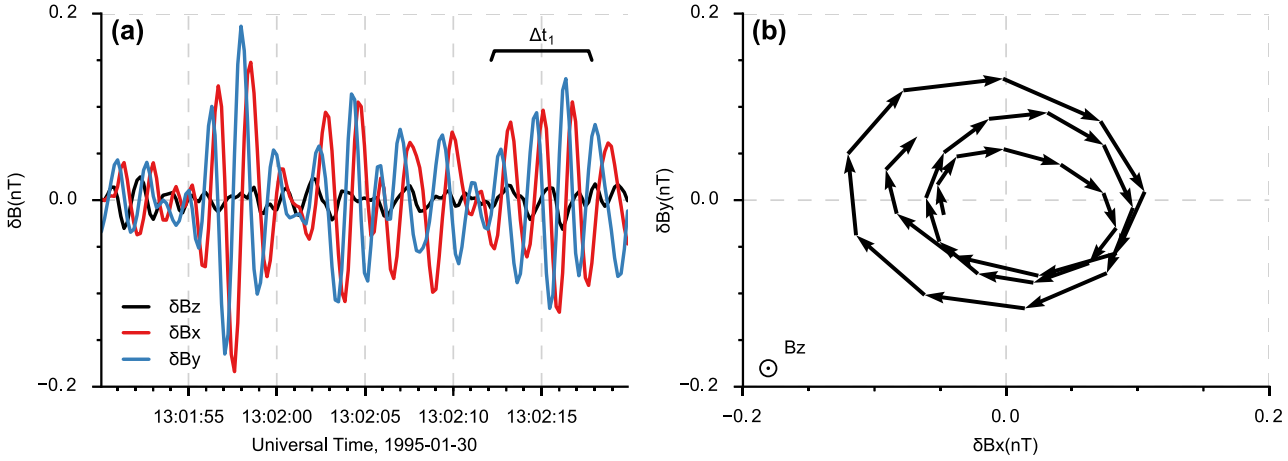

Figure 4. An example (30 s zoom) of coherent AIC wave observed by *Wind* on 1995 January 30 during the analyzed time interval. Left panel: magnetic field fluctuations within the frequency range [0.4, 1] Hz in the frame aligned with the local field, with $\boldsymbol{B}_0$ along $\boldsymbol{e}_z$. Right panel: left-handed polarization in the plane perpendicular to $\boldsymbol{B}_0$ represented as a hodogram.

the minimum eigenvalue is very small compared to the maximum one ($\lambda_{\min}/\lambda_{\max} \sim 10^{-3}$), i.e., $\boldsymbol{e}_{\min}$ is well defined.

In addition, as shown in Figure 1, during the two wave events (gray filled bands), the temperature anisotropy increases while $\beta_\parallel$ decreases. Here $T_\perp/T_\parallel \simeq 3.5$ and $\beta_\parallel \simeq 0.2$, which is compatible with AIC instability (Gary & Lee 1994) and in accordance with the growth rates between $\gamma_{\max} = 10^{-3}\omega_{ci}$ and $\gamma_{\max} = 10^{-1}\omega_{ci}$ (Hellinger et al. 2006). The generation of these low-frequency waves by AIC instability due to a temperature anisotropy seems a plausible scenario. Our analysis thus suggests that these waves are parallel ion cyclotron Alfvén waves.

Figure 5 shows two examples of magnetic fluctuations around the high-energy events that span a large range of scales in the scalograms of Figures 3(a) and (b) (at 13:29:45 and 13:42:25 UTC). Note that these are only two examples among others with similar characteristics and they were chosen primarily because of their well defined shapes. The upper panels show magnetic raw data projected to the minimum variance frame whereas the lower panels show the magnetic fluctuations $\delta\boldsymbol{B}$ (in the same reference frame). The fluctuations are defined (Equation (2)) between $f_{\min} = 0.06$ and $f_{\max} = 0.6$ Hz for panel (c), and between $f_{\min} = 0.1$ and $f_{\max} = 0.4$ Hz for panel (d); these ranges represent, respectively, the frequencies (or scales) where the events have their main contribution to the signal.

One can see that the magnetic data in the left panels correspond to a current sheet with an amplitude of $\delta B/B_0 \sim 0.75$. The angle $\theta_{BV} = 140°$ is oblique, $\boldsymbol{B}_0$ and $\boldsymbol{e}_{\min}$ are almost parallel ($\theta_{e\,\min,B} = 4°$) whereas $\boldsymbol{B}_0$ and $\boldsymbol{e}_{\max}$ are perpendicular ($\theta_{e\,\max,B} = 90°$). It seems that the current sheet is aligned with the mean magnetic field and the largest gradient is along the perpendicular direction. From the plot of fluctuations we estimate an upper bound for a temporal thickness of the current sheet. The principal gradient is within [1−3] s see Δt_2 in Figure 5(c)), which is of the same order as $f_b^{-1} \simeq 2.3$ s. The whole structure covers approximately 7 s. Assuming that this structure is convected by the solar wind, one can estimate its size using the projection of the velocity on the maximum variance axis $V_{e\,\max} = |\boldsymbol{V}_0 \cdot \boldsymbol{e}_{\max}| \sim 300\ \mathrm{km\,s^{-1}}$. Therefore, the scale of the gradient is [300-900] km, or [2.4-7.3] λ_i and [2.8-8.3] ρ_i. The largest scale of the structure is of the order of 2.1×10^3 km, or 17 λ_i and 19.4 ρ_i, which can be considered as a scale where the current sheet affects the surrounding plasma.

Figure 5, right panels, presents magnetic fluctuations that look like a wave packet of high amplitude ($\delta B/B_0 \sim 0.60$). The principal fluctuations are in the plane perpendicular to $\boldsymbol{B}_0$ ($\theta_{e\,\max,B} = 93°$, $\theta_{e\mathrm{med},B} = 87°$, $\theta_{e\,\min,B} = 5°$) and the field-to-flow angle is oblique, $\theta_{BV} = 140°$, as in the example of the current sheet. Different models can explain fluctuations of this kind, such as envelope soliton models (Ovenden et al. 1983; Buti et al. 2000) or the Alfvén vortex model (Petviashvili & Pokhotelov 1992).

Envelope soliton models describe fluctuations with $k_\parallel \gg k_\perp$. These wavevectors can be observed when $\boldsymbol{B}$ and $\boldsymbol{V}$ are aligned ($\theta_{BV} \sim 0$), as in the case of the AIC waves described above. Here, we are in an oblique configuration, $\theta_{BV} = 140°$ (or 40°), and, at the same time, the amplitudes of fluctuations are much higher than in the aligned case ($\theta_{BV} \sim 0$). If the solar wind turbulence is composed of a 2D component ($k_\perp \gg k_\parallel$) and a slab component ($k_\parallel \gg k_\perp$), as was suggested by Matthaeus et al. (1990), then in the oblique θ_{BV} configuration we will observe projections of these two components on the flow direction $\boldsymbol{V}$ of solar wind. However, as Horbury et al. (2008) and Wang et al. (2016) show, the 2D component has high amplitudes of fluctuations, and the slab component has much lower amplitudes (at $f < 1$ Hz). Therefore, the projection of the 2D component will dominate the projection of the slab for oblique angles θ_{BV}. So, it seems that the high-amplitude fluctuations we observe here in the oblique θ_{BV} configuration have $k_\perp \gg k_\parallel$, and it is reasonable to consider the Alfvén vortex model. Moreover, similar fluctuations on almost the same scales have already been observed by four *Cluster* satellites in the Earth's magnetosheath and have been interpreted as Alfvén vortices (Alexandrova et al. 2006).

Let us now verify whether the Alfvén vortex model (Petviashvili & Pokhotelov 1992) can explain our observation. The magnetic field components of the Alfvén vortex can be derived from the vector potential $\boldsymbol{A}$ given by Alexandrova

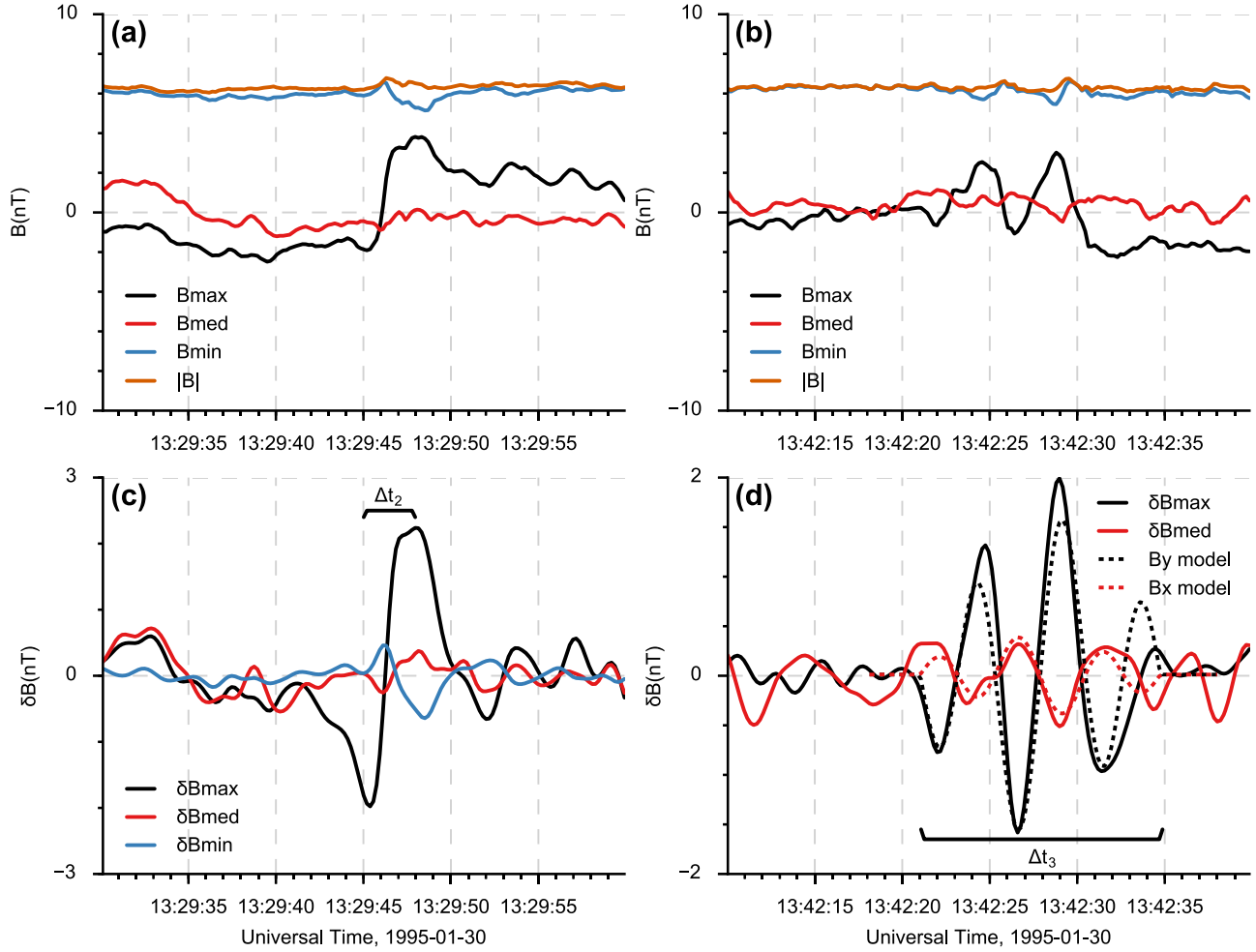

Figure 5. Two examples of coherent energetic events presented in the minimum variance frame calculated over time intervals of 30 s shown here. Left panels: current sheet detected at 13:29:46: (a) raw data, (c) fluctuations defined by Equation (2) in the frequency range [0.06, 0.6] Hz; duration $\Delta t_0 \simeq 3$ s. Right panels: signatures of an Alfvén vortex-like structure at 13:42:27: (b) raw data, (d) fluctuations defined in the frequency range [0.1, 0.4] Hz superposed on the monopole Alfvén vortex model from Petviashvili & Pokhotelov (1992); duration $\Delta t_3 \simeq 14$ s.

(2008):

$$\begin{cases} B_x(x,\,y) &= y\left(\dfrac{2\alpha x J_2(kr)}{r^2 J_0(ak)} - \dfrac{A_0 k J_1(kr)}{r}\right),\ r < a \\ B_x(x,\,y) &= -\dfrac{2a^2\alpha x y}{r^4},\ r \geqslant a \end{cases}$$

$$\begin{cases} B_y(x,\,y) &= \dfrac{2\alpha x^2 J_0(kr)}{r^2 J_0(ak)} - \dfrac{2\alpha(x^2-y^2)J_1(kr)}{kr^3 J_0(ak)} \\ & \quad -\alpha + \dfrac{A_0 k x J_1(kr)}{r},\ r < a \\ B_y(x,\,y) &= \dfrac{a^2\alpha(x^2-y^2)}{r^4},\ r \geqslant a. \end{cases} \quad (3)$$

Here A_0 is a constant amplitude, J_i is the Bessel function of ith order, $r = \sqrt{x^2+y^2}$ is the radial variable in the plane of the vortex, and $\alpha = \tan\gamma$, with γ the angle between the normal to the plane $(x,\,y)$ and $\boldsymbol{B}_0$. The vortex radius a represents the radius of the circle where the fluctuations are concentrated. To ensure the continuity of the magnetic field components at $r = a$, k is chosen to be one of the roots $j_{1,l}$ of J_1. The comparison is done in Figure 5(d), for $k = j_{1,3} \simeq 10.17$, $A_0 = 0.27$ in normalized units, and $\alpha = 0$, i.e., the Alfvén vortex has a monopole topology and it is static in the plasma frame. This fitting corresponds to the trajectory of the satellite across the center of the vortex, with a small angle of 13° to the direction of the intermediate variance $\boldsymbol{e}_{\rm med}$ (or the x-axis of the vortex model).

One can see that the monopole Alfvén vortex model (dashed lines in Figure 5(d)) fits the observations (solid lines) well. The small deviations can come from (i) the fact that the filter (Equation (2)) is far from ideal, and (ii) a superposition of the neighboring events on the studied vortex-like structure.

We estimate the radius of the vortex a (that is half the extent of magnetic fluctuations that are fitted to the vortex model) to be $\Delta t_3/2 \sim 7$ s. The scale of the strongest gradient within the vortex (scale of the central field-aligned current filament) is of the order of $\tau = 2$ s. Thus, the temporal scales of the vortex are around the break scale $f_b^{-1} \simeq 2.3$ s. Using the projection of the solar wind velocity on the vortex plane $(x,\,y) = (\boldsymbol{e}_{\rm max}, \boldsymbol{e}_{\rm med})$, 450 km s^{-1}, we obtain the vortex radius $a \sim 3150$ km or 25.4 λ_i and 29.2 ρ_i; and the scale of the strongest gradient $\ell \sim 900$ km or 7.3 λ_i and 8.3 ρ_i.

However, in order to have confidence in the interpretation in terms of the Alfvén vortex, a multi-satellite analysis should be

performed. This will be a subject of our future work. Here, we focus on the question of how the observed events such as AIC waves and coherent structures close to f_b influence the spectrum on ion scales.

4. INFLUENCE OF COHERENT EVENTS ON THE TURBULENT SPECTRUM

To determine how coherent processes such as quasi-monochromatic waves and coherent structures affect the turbulent spectrum around ion scales, we propose to separate coherent events from the rest of the signal in order to estimate their respective contribution to the total spectrum. We will separate (or filter) our data on the basis of the level of coherency, i.e., phase coupling, between two magnetic field components. For this, we use the wavelet coherence technique (Grinsted et al. 2004), applied previously in neuroscience and for geophysical time series to examine relationships in time–frequency space between two time series. The details are given in Appendix B.

As we have just seen, ion cyclotron waves are plane waves propagating parallel to the mean magnetic field with a phase coupling between the two perpendicular components B_x and B_y as shown in Figures 3(d) and 4. Coherent structures appear in the perpendicular scalogram (Figure 3(a)) and the parallel one (Figure 3(b)). As a consequence, the study of the phase coherence in the plane perpendicular to $\boldsymbol{B}_0$ can reveal the presence of waves, while the same technique applied to parallel and perpendicular components should highlight coherent structures.

To keep an equivalent number of events after filtering and obtain a spectrum with statistical properties close to those of Figure 2, we consider for the rest of the study the total interval of Figure 1, i.e., the central interval (1 hr) plus 30 minutes on each side.

Figure 6 presents the phase coherency $R_{ij}(f, t)$ (see Equation (9) in Appendix B) between B_i and B_j as a function of time and frequency. The top panel of Figure 6 corresponds to $R_{xy}(f, t)$ and the bottom panel to $R_{xz}(f, t)$. Low levels of coherency ($R_{ij}(f, t)$ close to zero) correspond to light areas on these maps and high levels of coherency ($R_{ij}(f, t)$ close to one) are dark areas: we will call them coherent areas.

For $R_{xy}(f, t)$, coherent areas are essentially in the frequency range close to or higher than f_b, whereas for $R_{xz}(f, t)$ they extend over almost all the frequencies and end on frequencies close to or above f_b.

The filtering is done, using the coherence maps of Figure 6, by selecting coherent areas above a threshold $R_{ij}^{\rm threshold}$ (see Equation (10) in Appendix B) at the break frequency f_b.

To help the reader to better visualize how the selection is made, we show in Figure 7 a cut of the coherency map $R_{xz}(f, t)$ between 13:25:00 and 13:30:00 UTC at $f = f_b$. $R_{xz}^{\rm threshold}$ is given by the blue filled area. The sets of coherent and non-coherent times correspond to $R_{xz}(f_b, t)$ above the threshold (red line) and below the threshold (black line), respectively. For comparison, the dashed line shows the average coherency over the different random signal realizations $\bar{R}_{xz}^{\rm random}(f_b, t)$. Then coherent times are used to calculate individual spectra of coherent events, and non-coherent times are used for the spectra of non-coherent fluctuations. For more information see Appendix B.

The resulting individual spectra are shown in Figure 8 (middle panels) together with an average coherence as a function of the frequency $\langle R_{ij}(f, t)\rangle_t$ (top panels) and the local slopes of the corresponding spectra[1] (bottom panels).

The average coherence gives information on the frequency localization of coherent events. Figure 8(top, left) gives this information for coupling of the components B_x–B_y: $\langle R_{xy}(f, t)\rangle_t$ is plotted as a solid red line and it is compared to $\langle R_{xy}^{\rm random}(f, t)\rangle_t$ (blue dashed lines); $\langle R_{xy}^{\rm threshold}(f, t)\rangle_t$ is indicated by the blue filled area. One observes an increase in $\langle R_{xy}(f, t)\rangle_t$ just below $f_b \simeq 0.4$ Hz and a maximum of $\langle R_{xy}(f, t)\rangle_t = 0.46$ around $f = 0.8$ Hz. This frequency range corresponds to the AIC waves.

The average coherence between B_x and B_z (Figure 8 (top, right)) exhibits a plateau $\langle R_{xz}(f, t)\rangle_t \sim 0.5$ between $f = 5 \times 10^{-2}$ Hz and $f = 0.9$ Hz (see the two vertical black arrows). This increase in coherency over a large frequency range corresponds to the presence of coherent structures, mainly current sheets and vortex-like structures, over all these scales, as discussed in Section 3. Note that, in this representation, it becomes clear that the smallest scale of the coherent structures is the local maximum at 0.7 Hz close to the right end of the plateau of the average coherency $\langle R_{xz}(f, t)\rangle_t$, i.e., in the vicinity of f_b. Here, results close to 1.6 Hz and beyond are to be interpreted with caution since we do not know the exact contribution of the noise. Finally, the effects of instrumental filters on the signal phase and coherence for frequencies near the Nyquist frequency remain to be determined.

Let us now consider the individual spectra and compare them to the original spectrum for the whole time interval (or global spectrum)—see the central panels of Figure 8. Here the spectrum of coherent and non-coherent fluctuations $E^{\rm c}$ and $E^{\rm nc}$ are, respectively, shown by blue and red solid lines. Note that they are normalized according to their respective contribution to the global spectrum (in black).[2]

Here, one observes that the spectra of non-coherent fluctuations do not exhibit any break. Also, the non-normalized individual spectra (not shown) of coherent events are higher than global and non-coherent spectra within the frequency ranges where the coherency increases (see top panels), i.e., around f_b, for (B_x, B_y) and between f_{ci} and $f_{\rho i}$ for (B_x, B_z). This result is consistent with the scalograms in Figure 3, which show that coherent structures are among the most energetic events of the interval.

The left panels of Figure 8 show that waves affect the local spectrum, creating a surplus of energy around their frequency, which results in a small bump (or a knee) around f_b in the coherent spectrum (in blue).

The right panels of Figure 8 show that the spectrum of coherent structures $E^{\rm c}$ (in blue) has a more pronounced break at f_b than the global spectrum (in black). $E^{\rm c}$ starts to deviates from the global spectrum at $f \geqslant f_{ci}$ (see bottom panel). In the inertial range ($f < f_{ci}$), the coherent spectrum is flatter than the non-coherent one with local slopes of $\alpha_{\rm c}(0.077\ {\rm Hz}) \simeq -1.5$ and $\alpha_{\rm nc}(0.077\ {\rm Hz}) \simeq -1.7$, respectively; whereas around ion scales ($f \geqslant f_{ci}$), the local slope for the coherent spectrum,

[1] The local slope is computed as follows: we divide the logarithmic frequency axis into 10 intervals of equal length; the local slope is then obtained using a linear fit considering only the points within each interval.

[2] The spectrum over the whole time interval is

$$E^{\rm global}(f) = E^{\rm c}(f)\frac{N_{\rm c}}{N_{\rm tot}} + E^{\rm nc}(f)\frac{N_{\rm nc}}{N_{\rm tot}},$$

where $N_{\rm c/nc/tot}$ are the number of points used to calculate coherent, non-coherent, and global spectra, respectively.

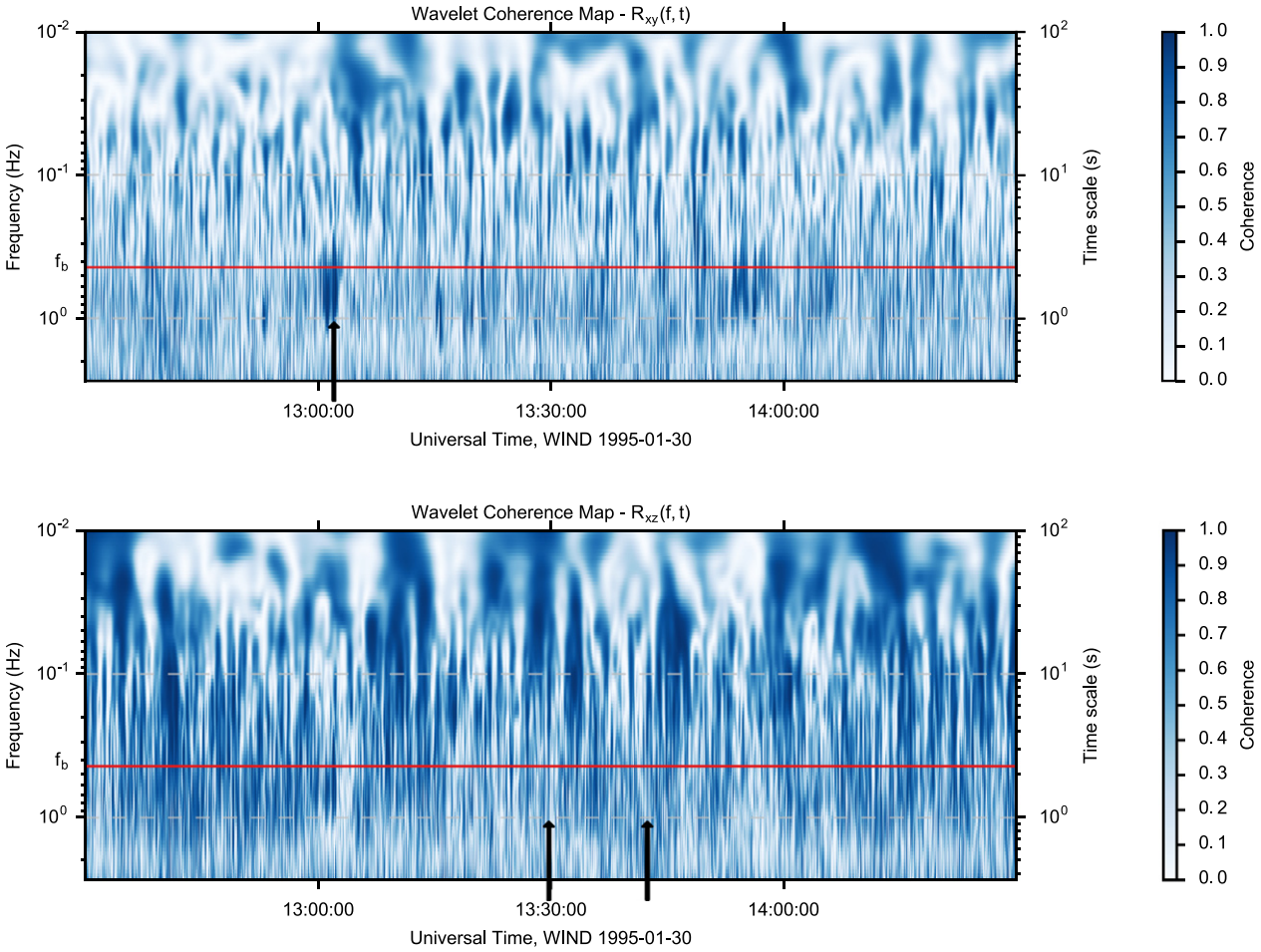

Figure 6. Maps of phase coherency $R_{ij}(t, f)$ between two magnetic field components B_i and B_j as a function of time and frequency. The red lines show the break frequency f_b. Upper panel: coherence between B_x and B_y components. Lower panel: coherence between B_x and B_z components.

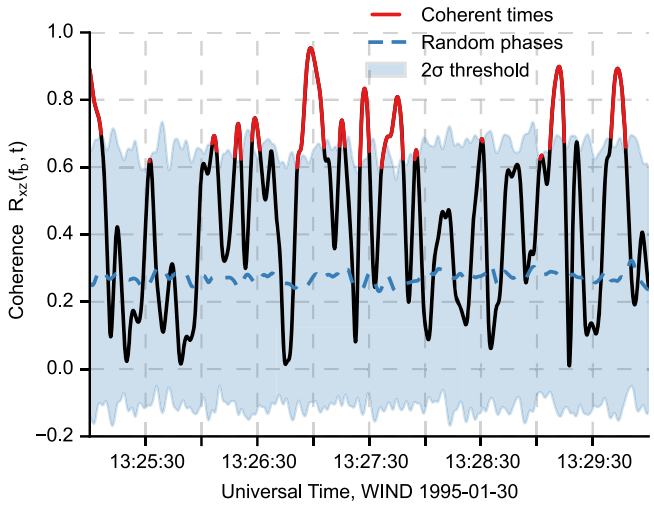

Figure 7. Cut of $R_{xz}(f, t)$, shown in the lower panel of Figure 6 at f_b. Here, red color corresponds to $R_{xz}(f_b, t)$ over the threshold (we refer to the corresponding times are coherent times); black corresponds to non-coherent times; the dashed blue line shows the mean value (over 100 realizations) of $R_{xz}(f_b, t)$, but for the random-phase surrogate signals; the filled area shows twice the standard deviation of the surrogate data.

$\alpha_c(0.6\,\mathrm{Hz}) \simeq -3.8$, is steeper than the non-coherent one, $\alpha_{nc}(0.6\,\mathrm{Hz}) \simeq -3.2$. The local slope of the global spectrum follows the slope of the coherent spectrum. Therefore we can deduce that the global scaling is imposed by the coherent part of the magnetic fluctuations. The coherent spectrum leads to a clear break because the structures cover a large number of frequencies up to their characteristic frequency, close to f_b. At f_b, their contribution to the spectrum drops drastically and the slope decreases sharply.

The spectra and their slopes also provide indications of the presence of Alfvén vortices. Indeed, Alfvén vortices have a specific spectral shape because of their magnetic topology (Alexandrova 2008). The magnetic field of a monopolar vortex is located within a circle of radius a (Petviashvili & Pokhotelov 1992). This creates a discontinuity in the current density at the edge of the vortex, which implies a spectrum f^{-2} for the current density. Therefore the magnetic field spectrum follows a power law of f^{-4}. So the $\sim f^{-4}$ spectrum at high frequencies ($f > f_b$) can be explained both by the discontinuous current spectrum of Alfvén vortices and by the lack of contribution from other structures.

The overall spectrum is an average of the coherent and non-coherent areas, whose shape depends partly on the percentage of coherent events in the interval. We define the percentage of coherent events for a given couple of magnetic field components (B_i, B_j) as the ratio between coherent and total times. It follows that the contribution of ion cyclotron waves in the global spectrum is of the order of 20%, lower than the contribution of coherent structures (around 40%).

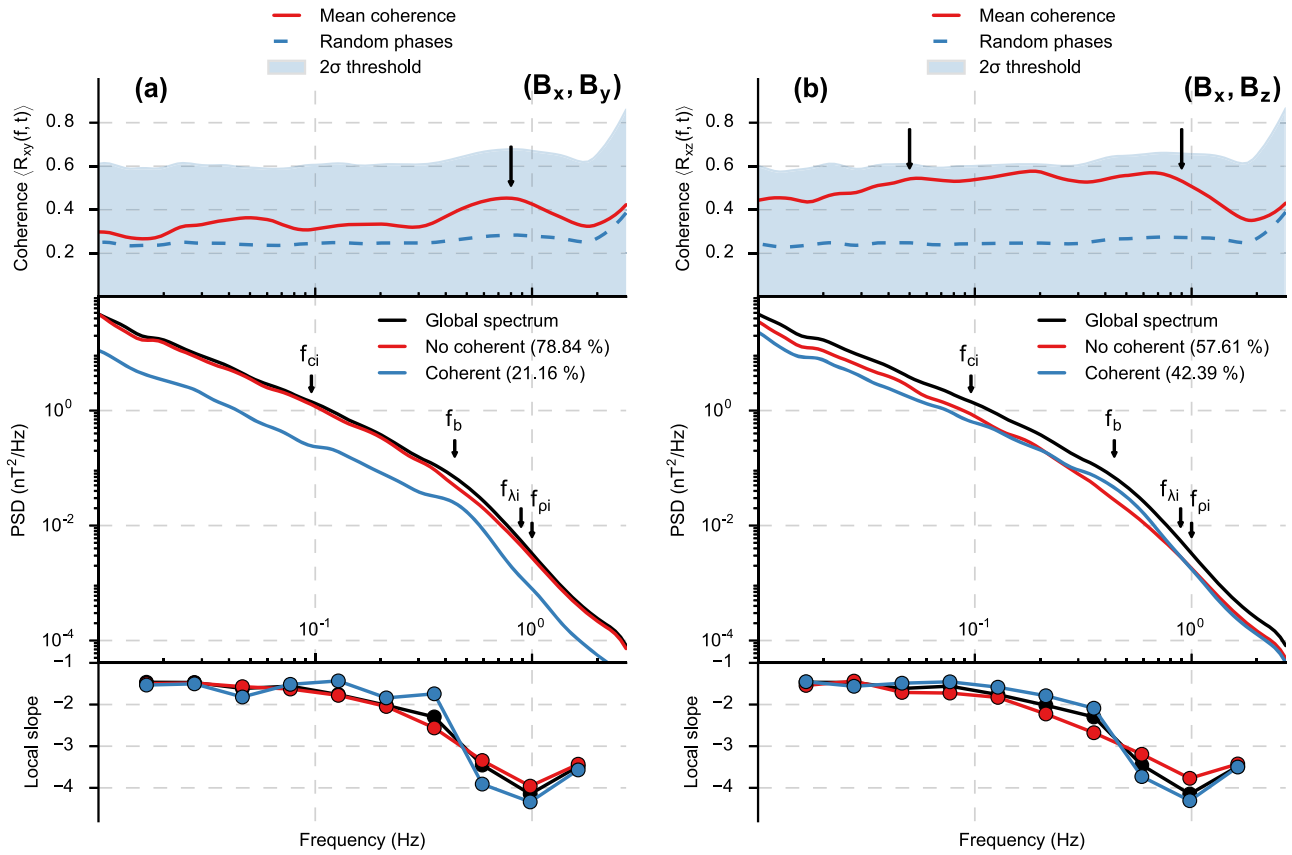

Figure 8. Coherence and spectra as functions of frequency for the couple (B_x, B_y) (left panels) and the couple (B_x, B_z) (right panels). Upper panels: averaged coherence over time (solid red), mean and twice the standard deviation of surrogate data (blue dashed line and filled area). Center panels: spectra over the whole interval (black), filtered spectra for the coherent (blue) and non-coherent (red) parts of the signal normalized according to their respective contribution to the global spectrum. Lower panels: local slopes corresponding to spectra in the center panels (same color code).

Figures 9 and 10 summarize our findings regarding the turbulent spectrum around ion scales in the fast solar wind stream studied here: it results from the superposition of waves (solid blue), coherent structures (solid red), and non-coherent fluctuations (solid orange). Spectra in the lower panel of Figure 9 are normalized according to their respective contribution to the global spectrum (as was done in Figure 8) while those of the upper panel are not.

The non-coherent and unpolarized fluctuations have a spectrum without any break. It can be modeled by a power law multiplied by an exponential cut-off $E(f) = E_0 f^{\alpha} \exp(-f/f_0)$, with $E_0 = 6.4 \times 10^{-2}$ (considering frequencies in Hz and the magnetic field in nT), $\alpha = -1.46$, and $f_0 = 0.31$ Hz (see the dashed black line for the fit). This model describes the evolution of the whole spectrum over three decades with a minimum number of free parameters. It is better seen from the compensated spectrum of non-coherent fluctuations, shown in Figure 10 by the black solid line (the other compensated spectra are shown here as well). One can see that it is flat over all measured frequencies, between 3×10^{-3} and 2 Hz, indicating that the model works quite well. However, the frequency range above the exponential cut-off frequency ($f > f_0$) is not large enough for us to be conclusive about the meaning of this adjustment and it will be necessary to consider both numerical simulations and observations over an extended frequency range to clearly understand the phenomena at work and estimate whether this exponential decay is due to any kind of dissipation.

5. SUMMARY AND CONCLUSION

In this paper, we tried to understand which physical phenomena govern the transition between inertial and kinetic ranges and why this transition is highly variable. To address these questions, we selected an interval of fast solar wind for which the spectrum exhibits a clear spectral break and a very steep slope of −4 at smaller scales (up to the noise level of the *Wind*/MFI instrument at 2–3 Hz). The choice of this interval was made in order to determine the conditions that give this specific spectral shape, not always observed in the solar wind.

Our analysis, based on phase coherency in time and scales calculated using the Morlet wavelet transform, shows the coexistence of (i) narrow-band incompressible left-handed circularly polarized waves with a central frequency at the spectral break frequency f_b; (ii) coherent events in the form of current sheets and Alfvén vortex-like structures with characteristic scales close to f_b, but covering a wide range of frequencies $\sim[5 \times 10^{-2}, 1]$ Hz starting one decade before f_b in the inertial range; (iii) a non-coherent and unpolarized component of turbulence.

A detailed multi-instrumental analysis shows that the circularly polarized waves are observed when the angle θ_{BV} between flow and field is close to zero. They propagate nearly parallel to the mean magnetic field $\boldsymbol{B}_0$ (i.e., $k_{\parallel} \gg k_{\perp}$) and their appearance is consistent with (1) favorable conditions for the development of the AIC instability (low ion beta $\beta_i \simeq 0.2$ and high ion temperature anisotropy $T_{\perp}/T_{\parallel} \simeq 4$) and (2) a low background level of turbulence. The decrease of the

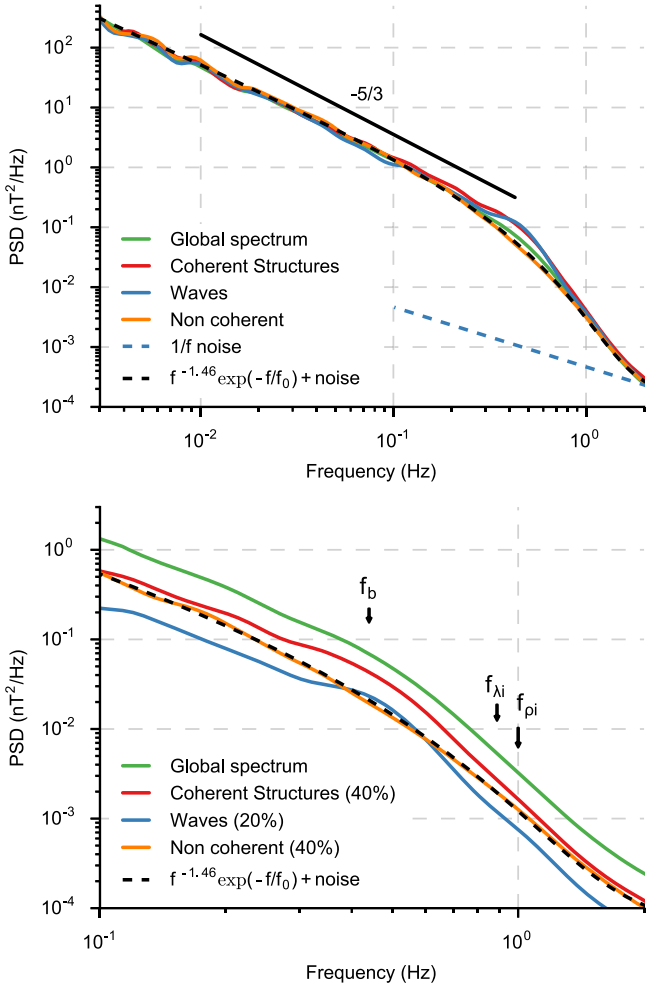

Figure 9. Decomposition of the ionic transition spectrum. Upper panel: global spectrum (solid green); filtered spectra for wave signatures (solid blue), coherent structures (solid red), and non-coherent parts (solid orange); $1/f$ noise (dashed blue); exponential fit for the non-coherent part (dashed black). Lower panel: zoom around the ion transition range, (0.1, 2) Hz, and normalization according to the respective contribution of each spectrum to the global one (same color code as the upper panel).

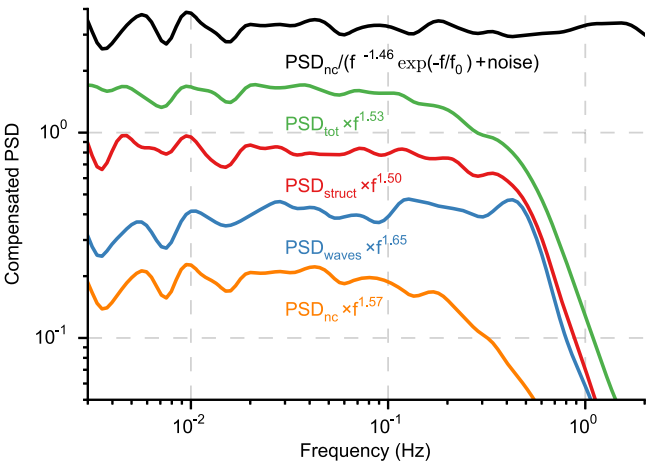

Figure 10. Compensated spectra of Figure 9: non-coherent spectrum compensated by the exponential fit (black) and each spectrum compensate by its respective power law in the inertial range for comparison (same color code as in Figure 9).

background can be a consequence of the alignment between $\boldsymbol{B}_0$ and the solar wind velocity during wave events (see Horbury et al. 2008; Podesta 2009). The individual spectrum containing only these AIC waves exhibits a bump in the spectrum around f_b.

The coherent structures observed here (particularly current sheets and Alfvén vortex-like structures) are also mostly Alfvénic, i.e., with principal fluctuations perpendicular to $\boldsymbol{B}_0$. However, they have a small compressible component with amplitude $\delta B_{\parallel} \ll \delta B_{\perp}$. Their geometry seems to be consistent with $k_{\perp} \gg k_{\parallel}$ anisotropy (however, to be sure, multi-satellite analysis should be done).

The presence of current sheets and magnetic vortices in plasma turbulence is not new: numerous numerical simulations show this. Current sheets are also widely observed in solar wind turbulence (e.g., Greco et al. 2010; Perri et al. 2012). However, regarding magnetic vortices, there are only a few examples of clear identification of such structures in space plasma turbulence. Alfvén vortices on the scale of the ion spectral break have been identified in the turbulence of the magnetosheaths of Earth and Saturn, just behind a quasi-perpendicular portion of the bow shocks (Alexandrova et al. 2006; Alexandrova & Saur 2008). Kinetic Alfvén vortices at smaller scales have been observed in the Earth's cusp region by Sundkvist et al. (2005). Signatures of large-scale Alfvén vortices (timescale ~3 minutes, i.e., $f \ll f_b$) in the fast solar wind have been reported by Verkhoglyadova et al. (2003). Roberts et al. (2013) showed an indirect indication of the presence of such vortices at ion scales: the authors applied a k-filtering technique for a time interval of a fast wind stream and obtained a dispersion relation that can be interpreted as oblique kinetic Alfvén waves or as convected structures, such as Alfvén vortices. Here, we clearly show the presence of high-amplitude localized magnetic fluctuations at ion scales that can be described by an Alfvén vortex model (Petviashvili & Pokhotelov 1992). These observations may indicate that intermittency in the solar wind turbulence is related not only to planar structures (like current sheets) but that there may also be filamentary structures like vortices.

The observed vortex-like structures are among the most energetic structures in the signal, so one cannot neglect their influence on the observed total spectrum with a clear break and a -4 power law at smaller scales. As was shown in Alexandrova (2008), the monopole Alfvén vortex has a current discontinuity on its boundary and this gives a spectrum of the current with a -2 power law at scales smaller than the vortex radius. This corresponds to a -4 spectrum of magnetic field, as far as $\boldsymbol{j} = \boldsymbol{\nabla} \times \boldsymbol{B} \sim kB$. At large scales, the vortex spectrum is flat and it has a knee at the scale of its radius. Indeed, as we show in the present study, the individual spectrum of the coherent structures exhibits a flattening at $f < f_b$, a clear knee at f_b, and -4 power law at $f > f_b$, consistent with the spectral properties of a monopole Alfvén vortex. Even if the coherent spectrum is similar to that of the vortex, we must not neglect the role of other structures. Indeed, the sharp drop in the power spectrum can be seen not only as the contribution of the discontinuous current spectrum of Alfvén vortices but also as the consequence of the lack of contribution from other coherent structures.

The third component of turbulence present in the analyzed time interval is neither coherent nor polarized, and it does not exhibit a spectral break at f_b at all. Its individual spectrum decreases smoothly around ion scales and is well fitted by a

power law multiplied by an exponential cut-off, $E(f) \propto f^{\alpha} \exp(-f/f_0)$ with $\alpha = -1.46$ and $f_0 = 0.31$ Hz.

Consequently, ion scales cannot be described by a single physical process, and therefore it is impossible to associate only one characteristic scale with the break frequency f_b. In particular, this may also explain why different characteristic scales, such as ρ_i, λ_i (Chen et al. 2014), and the resonant wavenumber of AIC waves (Bruno & Trenchi 2014) fit f_b well.

The presence of this break itself seems to be strongly related to the proportion and amplitude of waves and coherent structures in the analyzed signal. The strong steepening with a -4 power law seems to be simply the mixed spectrum of all the structures and may also be an indication of the presence of Alfvén vortex monopoles. Therefore, following the results of Bruno et al. (2014) and Smith et al. (2006), the faster the solar wind (the stronger the energy transfer rate ϵ), the steeper the spectrum at $f > f_b$; one may assume that in the fast wind there are more Alfvénic structures such as Alfvén vortices (or maybe simply more intense structures at ion scales) than in the slow wind, and the energy transfer rate is enhanced in the presence of these structures.

It will be interesting to analyze the role of the observed coherent structures in the problem of ion heating (Smith et al. 2006; Matthaeus et al. 2008), as already observed, for example, for much larger magnetic structures (hourly timescales); see for example Khabarova et al. (2015).

To summarize, the variety of spectral shapes observed in the solar wind around ion scales can be explained by different numbers, intensities, and durations of coherent events, such as waves and coherent structures, which themselves depend upon local plasma parameters (for waves) and non-local generation processes (for coherent structures).

It is important to clarify the limitation of our study. As the coherency technique detects only phase-correlated oscillation between magnetic field components, this method can miss events that appear only in one magnetic field component. We wish to emphasize as well that the present study is done for only 2 hr of data in the fast solar wind. To arrive to firm conclusions, a larger statistical study of the link between the phase coherence of turbulent fluctuations and spectral shape should be done. This will be a subject of our future work.

The authors would like to thank the anonymous referee for constructive comments that greatly improved the manuscript. We are also grateful to Petr Hellinger and Thierry Passot for their comments on the manuscript, and we would like to thank Denise Perrone, André Mangeney, Catherine Lacombe, Andrea Verdini, and Milan Maksimovic for useful discussions. The *Wind* data were obtained from the GSFC/SPDF CDAWeb interface at http://cdaweb.gsfc.nasa.gov/. The *Wind* MFI and SWE team are gratefully acknowledged for the magnetic field and proton data. This research made use of NASA's Astrophysics Data System, as well as matplotlib, a Python library for publication-quality graphics (Hunter 2007) and SciPy (Jones et al. 2001).

APPENDIX A
CONTINUOUS WAVELET TRANSFORM: SPECTRUM AND POLARIZATION

A.1. Spectrum and its Confidence Interval

A continuous wavelet transform (e.g., Farge 1992; Torrence & Compo 1998) allows one to obtain from a time series $B_j(t = t_i)$, with $t_i = t_0 + i\delta t$ and $i \in [|0, N-1|]$, the power spectral density (PSD) as a function of the frequency f in the spacecraft frame. This method has already been applied in previous studies (see, e.g., Alexandrova et al. 2008). Using the Morlet wavelet transform of the time series $B_j(t)$, we calculate the complex coefficient $W_j(f, t)$ as a function of the frequency in the spacecraft frame and the time t. The total PSD, i.e., the sum of the PSD of three components, is then written as

$$E(f) = \sum_{j=(x,y,z)} \frac{2\delta t}{N} \sum_{i=0}^{N-1} |W_j(f, t_i)|^2 = \sum_{j=(x,y,z)} 2\delta t \, \langle |W_j(f, t)|^2 \rangle_t . \quad (4)$$

It is then necessary to determine whether the wavelet spectrum is a good estimation of the true spectrum (and determine error bars for the wavelet spectrum). To do so, let $\mathcal{W}^2(f, t)$ be the true wavelet power (the wavelet power in the ideal case) and $|W(f, t_i)|^2$ the estimated one (our measurements). Formally, the probability that the estimated power should be close to the true power is

$$P\left(\chi^2_{\nu,\alpha/2} < \nu \frac{|W(f,t)|^2}{\mathcal{W}^2(f,t)} < \chi^2_{\nu,1-\alpha/2}\right) = 1 - \alpha. \quad (5)$$

$\chi^2_{\nu,\alpha/2}$ represents the value at which the χ^2_ν cumulative distribution function with ν degrees of freedom equals $\alpha/2$ ($\nu = 1$ for real coefficients, $\nu = 2$ for complex coefficients) and where α is the desired significance ($\alpha = 0.05$ for the 95% confidence interval). The confidence interval for the wavelet power is then

$$\frac{\nu |W(f,t_i)|^2}{\chi^2_{\nu,1-\alpha/2}} < \mathcal{W}^2(t,f) < \frac{\nu |W(f,t_i)|^2}{\chi^2_{\nu,\alpha/2}}. \quad (6)$$

The wavelet spectrum is the average of more or less independent wavelet coefficients. Indeed, for the continuous wavelet transform, wavelet coefficients are correlated over a certain time that depends on the mother wavelet and which is characterized by the decorrelation length $\tau = \gamma s$ where s is the scale ($s = \frac{1}{1.03f}$ for the Morlet wavelet) and γ is the decorrelation factor ($\gamma = 2.32$ for the Morlet wavelet). This implies that if $\bar{\mathcal{W}}^2(f)$ is the true spectrum and $\bar{W}^2(f) = \frac{1}{N}\sum_{n=0}^{N-1} |W(f, t_n)|^2$ is the estimated wavelet spectrum then the spectrum confidence interval is given by

$$\frac{\bar{\nu}\bar{W}^2(f)}{\chi^2_{\bar{\nu},1-\alpha/2}} < \bar{\mathcal{W}}^2(f) < \frac{\bar{\nu}\bar{W}^2(f)}{\chi^2_{\bar{\nu},\alpha/2}}, \quad (7)$$

where $\bar{\nu} = \nu N \delta t/\tau$ is the new degree of freedom (Torrence & Compo 1998), which takes into account the number of coefficients used for averaging and the correlation between these coefficients, with δt the time step.

For 1 hr of *Wind*/MFI measurements in the solar wind, it gives for one component $0.86 < \frac{\bar{\mathcal{W}}^2}{\bar{W}^2} < 1.18$ at $f = 0.1$ Hz and $0.95 < \frac{\bar{\mathcal{W}}^2}{\bar{W}^2} < 1.05$ for $f = 1$ Hz. Note that the confidence interval decreases with frequency.

A.2. Polarization of Magnetic Fluctuations

As indicated above, the Morlet wavelet coefficients $W_j(f, t)$ are complex. The argument $\phi_j(f, t) = \arg(W_j(f, t))\,[2\pi]$ of the complex coefficients can be interpreted as the local phase of the signal at a time t and a frequency f (Grinsted et al. 2004). The relative phasing between two time series, for example $B_x(t)$ and $B_y(t)$, is given by $\Delta\Phi_{xy}(f, t) = \phi_x(f, t) - \phi_y(f, t)$. Let $\boldsymbol{e}_x$, $\boldsymbol{e}_y$, and $\boldsymbol{e}_z$ form a direct trihedron, then the relative polarization with respect to the z-axis is given by

$$\Delta\Phi_{xy}(f, t) = \begin{cases} \pi/2 & [2\pi] \rightarrow \text{right handed} \\ 0 & [\pi] \rightarrow \text{linear} \\ -\pi/2 & [2\pi] \rightarrow \text{left handed.} \end{cases} \quad (8)$$

APPENDIX B
WAVELET TRANSFORM COHERENCE AND PHASE FILTERING

Two signals are said to be coherent if they maintain a fixed phase relationship. We use the wavelet transform coherence (WTC, see Grinsted et al. 2004) to separate coherent areas of the signal. The WTC highlights local phase-lock behavior and provides a good indication of the local correlation between the time series in the time–frequency space.

Let us consider two magnetic field components, $B_i(t)$ and $B_j(t)$, with $i, j = x, y, z$. The coherence coefficient $R_{ij}(f, t)$, which characterizes phase coupling between $B_i(t)$ and $B_j(t)$, is defined using the continuous wavelet transform of two signals:

$$R_{ij}^2(f, t) = \frac{|S(fW_i(f, t)W_j^*(f, t))|^2}{S(f|W_i(f, t)|^2) \cdot S(f|W_j(f, t)|^2)}, \quad (9)$$

where $W_{i(j)}(f, t)$ are complex wavelet coefficients of $B_{i(j)}(t)$ (Farge 1992), S is a smoothing operator defined by $S(W(f, t)) = S_{\text{freq}}(S_{\text{time}}(W(f, t)))$ with $S_{\text{freq}}(W(f, t)) = W(f, t)c_1^{-t^2f^2/2}$ the smoothing operator over frequencies, and $S_{\text{time}}(W(f, t)) = W(f, t)c_2\Pi(0.6/f)$ over time. c_1 and c_2 are numerically determined normalization constants (see Grinsted et al. 2004) and Π the rectangular function. The factor of 0.6 is the empirically determined scale decorrelation length for the Morlet wavelet (Torrence & Compo 1998). The normalization through the local average operator S allows one to consider not only the high-amplitude events with coupled phases, but all the phase-coupled events. By definition $R_{ij}(f, t)$ is between 0 (no coherence) and 1 (full coherence).

To remove the maximum of fortuitous coherence between two component (B_i, B_j) we need to determine the level of statistical significance of the WTC. For this purpose we construct N (=100) surrogate time series for each component from the original data, for which we randomize the phases as done in Hada et al. (2003) and Koga & Hada (2003). So, the significance threshold is defined as

$$R_{ij}^{\text{threshold}} = \overline{R}_{ij}^{\text{random}} + 2\sigma_{ij}^{\text{random}}, \quad (10)$$

using the mean

$$\overline{R}_{ij}^{\text{random}}(f, t) = \frac{1}{N}\sum_{k=1}^{N} R_{ij}^{(k)}(f, t), \quad N = 100 \quad (11)$$

and the standard deviation of the WTC for the 100 surrogate data sets

$$\sigma_{ij}^{\text{random}}(f, t) = \sqrt{\frac{1}{N}\sum_{k=1}^{N}(R_{ij}^{(k)}(f, t) - \overline{R}_{ij}^{\text{random}}(f, t))^2}. \quad (12)$$

If $R_{ij}^{\text{threshold}} > 1$, we take $R_{ij}^{\text{threshold}} = 1$ because R cannot be greater than 1.

We call coherent times T_{ij}^{c} the ensemble of time points such that two magnetic field components, $B_i(t)$ and $B_j(t)$, are coupled in phase at a fixed frequency f_0. These times are defined as the time set t that satisfies

$$R_{ij}(f_0, t) \geqslant R_{ij}^{\text{threshold}}(f_0, t). \quad (13)$$

The complementary set, T_{ij}^{nc}, corresponds to the non-coherent times.

The individual spectra of coherent (c) and non-coherent (nc) parts of the signal are then defined as

$$E_{ij}^{\text{c/nc}}(f) = \sum_{k=(x,y,z)} 2\delta t\,\langle|W_k(f, t)|^2\rangle_t, \text{ with } t \in T_{ij}^{\text{c/nc}}. \quad (14)$$

REFERENCES

Alexandrova, O. 2008, NPGeo, 15, 95
Alexandrova, O., Carbone, V., Veltri, P., & Sorriso-Valvo, L. 2008, ApJ, 674, 1153
Alexandrova, O., Chen, C. H. K., Sorriso-Valvo, L., Horbury, T. S., & Bale, S. D. 2013, SSRv, 178, 101
Alexandrova, O., Mangeney, A., Maksimovic, M., et al. 2006, JGRA, 111, 12208
Alexandrova, O., & Saur, J. 2008, GeoRL, 35, 15102
Bieber, J. W., Chen, J., Matthaeus, W. H., Smith, C. W., & Pomerantz, M. A. 1993, JGR, 98, 3585
Bourouaine, S., Alexandrova, O., Marsch, E., & Maksimovic, M. 2012, ApJ, 749, 102
Bruno, R., & Trenchi, L. 2014, ApJL, 787, L24
Bruno, R., Trenchi, L., & Telloni, D. 2014, ApJL, 793, L15
Buti, B., Velli, M., Liewer, P. C., Goldstein, B. E., & Hada, T. 2000, PhPl, 7, 3998
Chen, C. H. K., Leung, L., Boldyrev, S., Maruca, B. A., & Bale, S. D. 2014, GeoRL, 41, 8081
Farge, M. 1992, AnRFM, 24, 395
Farge, M., & Schneider, K. 2015, JPlPh, 81, 435810602
Frisch, U. 1995, Turbulence (Cambridge: Cambridge Univ. Press)
Gary, S. P., & Lee, M. A. 1994, JGR, 99, 11297
Greco, A., Matthaeus, W. H., D'Amicis, R., Servidio, S., & Dmitruk, P. 2012, ApJ, 749, 105
Greco, A., Servidio, S., Matthaeus, W. H., & Dmitruk, P. 2010, P&SS, 58, 1895
Grinsted, A., Moore, J. C., & Jevrejeva, S. 2004, NPGeo, 11, 561
Hada, T., Koga, D., & Yamamoto, E. 2003, SSRv, 107, 463
Hellinger, P., Trávníček, P., Kasper, J. C., & Lazarus, A. J. 2006, GeoRL, 33, 9101
Horbury, T. S., Forman, M., & Oughton, S. 2008, PhRvL, 101, 175005
Hunter, J. D. 2007, CSE, 9, 90
Jian, L. K., Wei, H. Y., Russell, C. T., et al. 2014, ApJ, 786, 123
Jones, E., Oliphant, T., Peterson, P., et al. 2001, SciPy: Open Source Scientific Tools for Python, http://www.scipy.org/
Khabarova, O., Zank, G. P., Li, G., et al. 2015, ApJ, 808, 181
Kiyani, K. H., Chapman, S. C., Sahraoui, F., et al. 2013, ApJ, 763, 10
Koga, D., & Hada, T. 2003, SSRv, 107, 495
Kolmogorov, A. 1941, DoSSR, 30, 301
Leamon, R. J., Matthaeus, W. H., Smith, C. W., et al. 2000, ApJ, 537, 1054
Leamon, R. J., Smith, C. W., Ness, N. F., Matthaeus, W. H., & Wong, H. K. 1998, JGR, 103, 4775
Lepping, R. P., Acũna, M. H., Burlaga, L. F., et al. 1995, SSRv, 71, 207
Markovskii, S. A., Vasquez, B. J., & Smith, C. W. 2008, ApJ, 675, 1576
Matthaeus, W. H., Goldstein, M. L., & Roberts, D. A. 1990, JGR, 95, 20673
Matthaeus, W. H., Weygand, J. M., Chuychai, P., et al. 2008, ApJL, 678, L141

Ogilvie, K. W., Chornay, D. J., Fritzenreiter, R. J., et al. 1995, SSRv, 71, 55
Ovenden, C. R., Shah, H. A., & Schwartz, S. J. 1983, JGR, 88, 6095
Parker, E. N. 1958, ApJ, 128, 664
Perri, S., Carbone, V., & Veltri, P. 2010, ApJL, 725, L52
Perri, S., Goldstein, M. L., Dorelli, J. C., & Sahraoui, F. 2012, PhRvL, 109, 191101
Petviashvili, V. I. V. I., & Pokhotelov, O. A. O. A. 1992, Solitary Waves in Plasmas and in the Atmosphere (Philadelphia: Gordon and Breach) translation of: Uedinennye volny v plazme i atmosfere
Podesta, J. J. 2009, ApJ, 698, 986
Roberts, O. W., Li, X., & Li, B. 2013, ApJ, 769, 58
Sahraoui, F., Goldstein, M. L., Belmont, G., Canu, P., & Rezeau, L. 2010, PhRvL, 105, 131101
Salem, C., Mangeney, A., Bale, S. D., & Veltri, P. 2009, ApJ, 702, 537
Salem, C. S., Howes, G. G., Sundkvist, D., et al. 2012, ApJL, 745, L9
Smith, C. W., Hamilton, K., Vasquez, B. J., & Leamon, R. J. 2006, ApJL, 645, L85
Sonnerup, B. U. Ö, & Scheible, M. 1998, ISSIR, 1, 185
Sundkvist, D., Krasnoselskikh, V., Shukla, P. K., et al. 2005, Natur, 436, 825
Taylor, G. I. 1938, RSPSA, 164, 476
Torrence, C., & Compo, G. P. 1998, BAMS, 79, 61
Veltri, P. 1999, PPCF, 41, 787
Verkhoglyadova, O. P., Dasgupta, B., & Tsurutani, B. T. 2003, NPGeo, 10, 335
Wang, X., Tu, C., Marsch, E., He, J., & Wang, L. 2016, ApJ, 816, 15
Wu, P., Perri, S., Osman, K., et al. 2013, ApJL, 763, L30
Zwillinger, D., & Kokoska, S. 2000, CRC Standard Probability and Statistics Tables and Formulae (New York: Chapman and Hall)